

Identification of Alpine Glaciers in the Central Himalayas Using Fully Polarimetric L-Band SAR Data

Guo-Hui Yao, Chang-Qing Ke¹, Xiaobing Zhou², Hoonyol Lee, *Senior Member, IEEE*, Xiaoyi Shen³, and Yu Cai

Abstract—To study the applicability of full polarimetric synthetic aperture radar (SAR) data to identify alpine glaciers in the central Himalayas, six polarimetric decomposition methods were used to obtain 20 polarimetric characteristic parameters based on the Advanced Land Observing Satellite 2 (ALOS-2) Phased Array type L-band SAR (PALSAR) data. Object-oriented multiscale segmentation was performed on a Landsat 8 Operational Land Imager (OLI) image prior to classification, and the vector boundaries of different types of training samples were selected from the segmented results. We performed a support vector machine (SVM)-based classification on the characteristic parameters from each polarimetric decomposition. All 20 parameters were then screened and combined according to different requirements: the degree of separability of different types of training samples and the type of scattering mechanisms. The results show that the classification accuracy of the incoherent decomposition characteristics based on the covariance matrix is the best, reaching 87%, and it can exceed 91% after adding the local incidence angle to the suite of classifiers. Eventually, more than 93% accuracy was achieved using a combination of multiple polarimetric parameters, which reduced the misclassification between bare ice and rock. We also analyzed the use of controlling factors on the accuracy of alpine glacier identification and found that the polarimetric information and aspect of the glacier surface are the most important factors. The former is the main basis for identification but the latter will confuse the feature distributions of different categories and cause misclassification.

Index Terms—Alpine glacier, local incidence angle, object-oriented segmentation, polarimetric decomposition, support vector machine (SVM).

Manuscript received November 24, 2018; revised May 7, 2019 and July 19, 2019; accepted August 28, 2019. Date of publication September 25, 2019; date of current version December 27, 2019. This work was supported in part by the Program for the National Natural Science Foundation of China under Grant 41830105 and in part by the International Scholar Exchange Fellowship (ISEF) Program at the Korean Foundation of Advanced Studies (KFAS). (Corresponding author: Chang-Qing Ke.)

G.-H. Yao, C.-Q. Ke, X. Shen, and Y. Cai are with the School of Geography and Ocean Science, Nanjing University, Nanjing 210023, China, with the Jiangsu Provincial Key Laboratory of Geographic Information Science and Technology, Nanjing University, Nanjing 210023, China, with the Key Laboratory for Satellite Mapping Technology and Applications of State Administration of Surveying, Mapping and Geoinformation of China, Nanjing University, Nanjing 210023, China, and also with the Collaborative Innovation Center of Novel Software Technology and Industrialization, Nanjing University, Nanjing 210023, China (e-mail: guohuiyao98@163.com; kecq@nju.edu.cn; 823273803@qq.com; caiyu13834585@163.com).

X. Zhou is with the Department of Geophysical Engineering, Montana Tech of the University of Montana, Butte, MT 59701 USA (e-mail: xzhou@mtech.edu).

H. Lee is with the Division of Geology and Geophysics, Kangwon National University, Chuncheon 24341, South Korea (e-mail: hoonyol@kangwon.ac.kr).

Color versions of one or more of the figures in this article are available online at <http://ieeexplore.ieee.org>.

Digital Object Identifier 10.1109/TGRS.2019.2939430

I. INTRODUCTION

THE Himalaya Mountains and the Tibetan Plateau, the “world’s third pole,” are often referred to as the “Water Tower of Asia.” Glacial meltwater from the Himalaya Mountains provides crucial freshwater resources to a larger number of people than any other mountain range in the world [1]. The accumulation and melting of snow and glacial ice can affect runoff at different time scales in the surrounding countries. Glaciers are among the most sensitive indicators of terrestrial climate variability and their variations can impact the local and regional climate [2], [3]. Accelerated movements and shrinking of glaciers in the Himalaya have been observed in recent years [4], [5]. Glacier monitoring has become necessary for assessing water resource availability for the surrounding countries and providing feedback on the regional climate.

The identification of glaciers is a very important component in glacier monitoring; georeferenced remote sensing images are used because the extracted boundaries of glaciers can indicate glacier variations, movement, and ice mass balance [6], [7]. Glaciers are usually difficult to access, and optical and microwave remote sensing images are thus widely used for glacier identification and monitoring.

Research on the identification of glaciers in the Himalaya has been carried out for decades [8]. In the early years, the main source of data was high-resolution optical images, and the normalized difference snow index (NDSI) was used. Spectral bands chosen for NDSI calculation vary across sensors: for Landsat Thematic Mapper (TM) images, band 3 and band 5 were used [9]–[15], while for Landsat 8 Operational Land Imager (OLI) images, band 3 and band 6 were used [14]–[17]. Thresholds of NDSI were set to extract glacier boundaries [15], [17]. The disadvantage of this method is that it is difficult to unify the threshold values used in different images acquired under different conditions. Glacier identification is often a process of continuous optimization of these thresholds. Moreover, optical imaging is limited by weather conditions. During the accumulation phase of the glaciers in the Himalayas, there are usually clouds, making it difficult to acquire a long-term sequence of cloudless satellite images with an appropriate temporal resolution.

Synthetic aperture radar (SAR) images are different from optical images; the penetration capacity of SAR through clouds makes it almost independent of weather in acquiring the information on the Earth’s surface. L-band SAR has a lower frequency and a longer wavelength than C- and X-band SAR

and can thus penetrate deeper through snow and ice and has a better coherence in glacial areas than C- and X-band SAR [18]. SAR data can be complex, consisting of real and imaginary parts, representing the backscattered intensity of the radar beam and the phase angle changes, respectively [19]. Applications of SAR to glacier monitoring involve applying both parts.

The use of SAR data to identify a glacial zone began in the late 1980s, using the sensitivity of single- and multipolarized radar waves to different glacier surface conditions, such as wetness and roughness, to distinguish between snow and glacier ice [20]–[23]. Later, several studies were carried out on glacier identification using classifiers based on the backscattering coefficient [24]–[26]. Using the SAR backscattering coefficient in identifying glaciers is dependent on the differences in the physicochemical properties of each feature in the glacial zone in the SAR images. Therefore, it is important to understand the surface features, internal structure, and chemical composition of the glaciers. For example, [27] used the radar backscattering dependence on the crystal size of glacier ice to monitor glacier zones and snow/firn line changes in the Tibetan Plateau. According to the difference in the dielectric constant caused by different water contents, dry and wet snow can be distinguished and snow lines can be extracted [28]. Calm water surfaces cause specular reflection and result in a very low backscattering coefficient in a SAR image. Therefore, glacial lakes can be easily identified [24]. The radar backscattering coefficient can be affected by surface roughness, which is a function of the local incidence angle and wavelength [29]. Debris on glacial ice in the ablation zone produces a rough surface that backscatters a substantial amount of radar signal back to the receiving antenna, which makes a glacier with debris cover very bright; thus, the glacier can be recognized relatively easily in a SAR image [30]. Due to the dynamic behaviors of glaciers, the scattering coefficient of various glaciers varies over time [27], reducing the identification accuracy of glaciers if only the radar backscattering coefficient is used.

The phase information in single-polarization SAR data can be used through the differential interferometric SAR (DInSAR) method. Interferometry is often used to detect dynamic deformations or movement, and thus, it is often used for flow-rate change detection and material balance studies in glaciology [31]. The flow and ablation of the surface of a glacier will cause SAR images acquired at different times to lose coherence; the difference in coherence coefficients can thus be used to distinguish a dynamic glacier from permanent surface features [32]. However, the DInSAR method has limitations: the viability of using InSAR to identify glaciers in alpine regions is often limited by the coherence loss over glacier surfaces when SAR image pairs with temporal baselines of more than one day are used [33]. When the time gap or spatial baseline is longer, the coherence of the image pair is compromised. Moreover, faster-moving glaciers are more prone to coherence loss. Thus, the requirement for the data acquisition time interval for InSAR is restrictive. Practically, the InSAR method is more suitable for relatively stable glaciers.

When a radar wave interacts with ground targets, the polarization state of the radar wave will change; the degree of

change is related to the dielectric constant, structure, roughness, and chemical composition of targets. The surface and volume components must be decomposed to infer separate information on the properties of the ice surface and interior. Polarimetric decomposition can quantify the contribution of the surface and volume backscattering, improving the ability to distinguish different glacial zones [34]. The characteristic parameters of polarimetric decomposition not only increase the information in a radar image but also expand the application dimension of SAR data in glacier remote sensing [25], [34]–[36]. Furthermore, polarimetric decomposition can be used to calculate the thickness of the debris covering the surface of a glacier [37]. It has been found that in identifying glaciers with polarized radar, factors such as the (local) incidence angle, polarization, and the underlying surface types must be considered [38]. In particular, the local incidence angle affects the surface roughness and the penetration depth and thus the radar backscattering signals. A large incidence angle can produce an underestimated target area [24]. In radar, as the depression angle of the radar beam decreases or the local incidence angle increases, the vertical relief of a surface to be considered rough increases [29], the penetration depth decreases, the transmission coefficient of surface scattering also decreases [39], and the influence of surface roughness on the scattering is stronger, which leads to the degree of polarization decrease, and further leads to the misclassification of wet snow and snow-free ground surfaces [40]. The addition of the local incidence angle to the suite of classifiers can effectively improve the classification accuracy [37], [40]. However, the past research activities on the use of SAR to identify glaciers focused mainly on supervised or unsupervised classification based on scattering coefficients, scattering characteristics, and polarimetric decomposition parameters, ignoring the important role played by the local incidence angle on the classification accuracy.

The objective of this article is to investigate how to improve the identification accuracy of glacial zones in the central Himalayas region using the multiresolution segmentation and target decomposition, especially for screening and combining a variety of polarimetric decomposition parameters and taking into account the local incidence angle. Additionally, we analyzed the source of errors and improved identification accuracy in the multiparameter classification process.

II. STUDY AREA AND EXPERIENTIAL DATA

A. Study Area

The study area is located on the eastern-facing side of Mount Everest, the highest peak in the world. It belongs to the central Himalaya region [5], and it includes typical middle-latitude and high-altitude glaciers. Precipitation is mainly controlled by the Indian and Southeast monsoons, with the latter contributing more than 80% of the annual rainfall [41]. The study area has a dry season from October to March [42]. Three glaciers are located in the area, with no debris coverage. The slope angles are $20^\circ \pm 5^\circ$ with azimuth angles varying from 0° to 360° [see Fig. 1(e)].

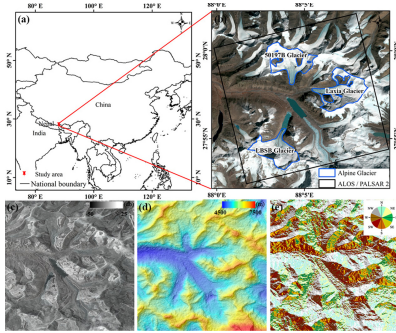


Fig. 1. (a) Regional map showing the location of the study area. (b) Location of the study area superimposed on a Landsat 8 OLI image (October 27, 2016). (c) Intensity image of HH polarization of ALOS PALSAR acquired on August 24, 2016. (d) GDEM (version 2) of ASTER acquired in 2011 corresponding to the SAR image coverage. (e) Aspect map derived from the DEM data.

Fig. 1(a) is a regional map that shows the study area, located near the boundary between Nepal and China. The enlarged map of the study area is shown in Fig. 1(b), which is a Landsat 8 OLI true-color image acquired on October 27, 2016, in which the three glaciers, i.e., the 50197B, Laxia, and LBSB glaciers, are labeled. The black rectangle shows the ground coverage of the SAR image used in this article. Fig. 1(c) shows the Advanced Land Observing Satellite 2 (ALOS-2)-Phased Array type L-band SAR (PALSAR) intensity image with HH polarization acquired on August 24, 2016. Fig. 1(d) shows that the elevation in the study area, which is between 4500 and 7500 m, with a visible distribution of peaks and valleys, and the aspect map obtained from the digital elevation model (DEM) data is shown in Fig. 1(e), in which different colors indicate different orientations of the mountains. Aspect, or simply the slope direction, refers to the downslope direction of the maximum rate of change in elevation from each pixel to its neighbors. It is measured clockwise from due north (0°) to due north again (360°): a full circle. Flat pixels with no downslope direction are given a value of -1 .

B. Satellite SAR Data

ALOS-2 full polarization data were used in this article. The PALSAR aboard the ALOS-2 satellite is a SAR sensor that transmits L-band radar waves and receives backscattered signals from the ground. Its capacity has been significantly improved from that of its predecessor, ALOS PALSAR, in terms of the spatial and temporal resolutions, observation band, modes of polarization, and time lag for data delivery. In particular, the full polarization mode can acquire all the polarimetric characteristics of a target, which greatly improves the acquisition ability of the target information of the imaging radar. This article used a quad-polarization SAR image of the high-sensitive category in the stripmap mode with a spatial resolution of 6 m. The imaging time was August 24, 2016, when glacier ablation was still active, wet snow and smooth ice surface lead to a large increase in dielectric constant in snow, and the backscattering coefficient was low [27].

To obtain training samples for the classification of glacier zones, a high-resolution Landsat 8 optical remote sensing

image was used for selecting the training samples for glacier zone classification. Theoretically, the optical image to be overlaid with the SAR image should be acquired at the same time as the SAR image. However, the cloud cover over the study area on August 24, 2016, when the SAR image was acquired, was thick, and the Landsat 8 optical image could not be used. Comparing the optical images acquired from May to October 2015, 2016, and 2017, we found that the boundaries of the glaciers in the study area were almost constant. Therefore, we used the Landsat 8 optical image with 30-m resolution acquired on October 27, 2016, which has only 4.09% cloud cover, as the optical image to be overlaid with the radar image for selecting training samples because this image is temporally the closest to the time the SAR image was acquired.

C. DEM Data

The Advanced Spaceborne Thermal Emission and Reflection Radiometer (ASTER) Global DEM (GDEM) data were first published by NASA in 2009; version 2 of the data was released in 2011. It has a spatial resolution of 30 m, the vertical accuracy of 20 m and a horizontal precision of 30 m. In this article, ASTER GDEM (version 2) data were mainly used for geocoding the SAR data and aspect data generation. The aspect data generated were used to calculate the local incidence angle of the radar beam on the glacier surface.

D. Second Glacier Inventory Data Set of China

The Second Glacier Inventory data set of China [43] was provided by the Cold and Arid Regions Science Data Center in Lanzhou, China (<http://westdc.westgis.ac.cn>). This data set is the result of a new survey of the distribution of glaciers in China after the first glacier inventory in 2002. The data center used Landsat TM, Enhanced TM Plus (ETM+), and Shuttle Radar Topography Mission (SRTM) version 4 data (2006–2011) as the main data sources. The glacier boundary of the bare ice area was extracted by ratio-threshold segmentation, and the glacier attributes were calculated by the international general algorithm [10], [44]–[47]. In this article, the glacier boundary from this data set is used as a spatial reference for the glacier identification results.

III. METHODS

The optical and SAR images were processed following the flowchart shown in Fig. 2. The entire procedure is subdivided into four main components: multiscale segmentation of the optical image, SAR data preprocessing, polarimetric decomposition, and support vector machine (SVM) classification.

A. Object-Oriented Segmentation of an Optical Image

Object-oriented multiscale segmentation makes use of the spectral and texture information of optical images. When applied to the Landsat 8 image, the segmented results can directly correspond to different types of features of the specific spectrum and generate corresponding segmentation vector boundaries, from which the pure pixels were selected as the training samples for SAR image classification.

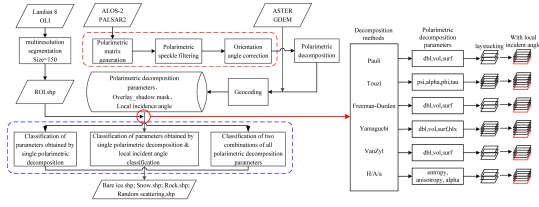


Fig. 2. Flowchart of data processing, including four parts: multiscale segmentation of Landsat 8 OLI image, preprocessing of full polarization SAR data (the red dashed box), target polarimetric decomposition and multiparameter classification (the blue dashed box). The content indicated by the red arrow shows the combination of parameters of each polarimetric decomposition method and how the local incidence angle is added to the classification process.

B. SAR Data Preprocessing

The preprocessing of the SAR data (the red dashed rectangle, Fig. 2) before polarimetric decomposition includes polarimetry matrix generation, polarimetric speckle filtering, and orientation angle correction. Each of these components is explained in detail below. The information of each pixel in a polarized radar image can be expressed by the complex Sinclair scattering matrix

$$S = \begin{bmatrix} S_{HH} & S_{HV} \\ S_{VH} & S_{VV} \end{bmatrix} \quad (1)$$

where $[S]$ is a 2×2 complex scattering matrix that describes the scattering phenomenon of scatterers on incident waves and S_{HV} represents the target backscattering coefficient of the transmitted horizontally (H) polarized wave and the received vertically (V) polarized wave. Then, to extract physical information from a scattering matrix, the matrix S can be converted into a target scattering vector k with the Lexicographic matrix basis

$$k = [S_{HH} \ S_{HV} \ S_{VH} \ S_{VV}]^t \quad (2)$$

where the superscripted t indicates matrix transposition. Based on the above equation, second-order products of the scattering matrix related to depolarization can be defined as, namely, the coherence matrix $[T_3]$ and the covariance matrix $[C_3]$ [48], [49], see (3) and (4), as shown at the bottom of this page, where the subscripted 3 indicates that the equation satisfies reciprocity and $(\cdot)^*$ stands for the complex conjugate of the quantity (\cdot) .

Speckle is a scattering phenomenon in SAR imaging that is caused by the random constructive and destructive interference of the backscattered waves by elementary scatterers within each pixel. Backscattered waves are not conducive to image interpretation and need to be suppressed by speckle filtering, which requires the consideration of speckle statistics.

For polarimetric SAR data, the complex Wishart distribution represented by a covariance or coherency matrix describes the speckle statistics well. To maintain the polarimetric characteristics, each element of the covariance matrix must be independently filtered in the spatial domain to avoid crosstalk between polarization channels. The improved Lee sigma filter [50] satisfies the above requirements by adopting the edge-aligned window and the filtering weights from the spanned image. It preserves both the sharpness and polarimetric information of a polarimetric SAR image while suppressing speckle noise.

Previous studies have shown that the backscattering of any surface is influenced by the dielectric constant, the surface roughness, and the local incidence angle [38]. In particular, if the surface norm is not in the incidence plane, the orientation angle shift δ is induced. Finally, the orientation angle shift δ is estimated using the circular polarization method and is removed from the polarimetric data. This procedure is called orientation angle correction.

C. Polarimetric Decomposition

To fully investigate the polarimetric characteristics of glaciers and compare the effects of different polarimetric decompositions on the classification of glacial zones, both coherent and incoherent polarimetric decompositions, including Pauli, Touzi, Freeman-Durden, Yamaguchi, Van Zyl, and $H/A/a$ decompositions, were chosen for processing.

The most relevant coherent scattering decomposition is Pauli decomposition [51], which expresses the measured scattering matrix S in terms of the Pauli basis, which maintains the total scattering power. In a monostatic case, where $S_{HV} = S_{VH}$, the measured scattering matrix can be divided into three basic matrices corresponding to canonical scattering mechanisms: the first part corresponds to the scattering from a sphere, a plate or a trihedron (simply called single- or odd-bounce scattering); the second and the third parts represent the scattering from a dihedral oriented at 0° (double- or even-bounce) and 45° (volume scattering), respectively [52].

Touzi decomposition is a unique, roll-invariant and incoherent decomposition method of target scattering [53]. To some extent, it is derived from coherent decomposition. Four parameters can be extracted after the characteristic decomposition of the coherency matrix T , and the new target scattering vector model is applied to each eigenvector. They represent four averaged parameters of roll-invariant parameters: maximum polarimetric parameter-orientation angle (Ψ), helicity (τ), magnitude (α), and phase (Φ) of the symmetric scattering [54].

Freeman-Durden decomposition is the best version of model-based incoherent decomposition. Freeman-Durden

$$T_3 = \frac{1}{2} \begin{bmatrix} |S_{HH} + S_{VV}|^2 & (S_{HH} + S_{VV})(S_{HH} - S_{VV})^* & 2(S_{HH} + S_{VV})S_{HV}^* \\ (S_{HH} - S_{VV})(S_{HH} + S_{VV})^* & |S_{HH} - S_{VV}|^2 & 2(S_{HH} - S_{VV})S_{HV}^* \\ 2S_{HV}(S_{HH} + S_{VV})^* & 2S_{HV}(S_{HH} - S_{VV})^* & 4|S_{HV}|^2 \end{bmatrix} \quad (3)$$

$$C_3 = \begin{bmatrix} |S_{HH}|^2 & \sqrt{2}S_{HH}S_{HV}^* & S_{HH}S_{VV}^* \\ \sqrt{2}S_{HV}S_{HH}^* & 2|S_{HV}|^2 & \sqrt{2}S_{HV}S_{VV}^* \\ S_{VV}S_{HH}^* & \sqrt{2}S_{VV}S_{HV}^* & |S_{VV}|^2 \end{bmatrix} \quad (4)$$

decomposition applies three scattering mechanisms to the covariance matrix: 1) canopy scattering from a cloud of randomly oriented dipoles, such as forests; 2) even- or double-bounce scattering from a pair of orthogonal surfaces (dihedral scatterers) with different dielectric constants; and 3) Bragg scattering from a moderately rough surface. It decomposes the original covariance or coherency matrix into a form of the weighted sum of volume, double-bounce, and surface or single-bounce scattering [55]. The double-bounce component of the covariance matrix is expected to depend on the dielectric constants of the surface. The total scattering power (P_T) includes contributions from volume scattering (P_V), double-bounce scattering (P_D), and surface scattering (P_S)

$$P_T = |S_{HH}|^2 + |S_{VV}|^2 + 2|S_{HV}|^2 = P_V + P_D + P_S. \quad (5)$$

Yamaguchi decomposition is an extension of Freeman-Durden decomposition that takes into account the helix scattering that is caused by the complex shape of artificial structures such as buildings and bridges. Therefore, the energy in urban areas is large, and in natural land cover areas, it is small [56]. The measured coherency matrix T can be divided into four parts corresponding to four submatrices

$$T = f_s T_{\text{surface}} + f_d T_{\text{double-bounce}} + f_v T_{\text{volume}} + f_c T_{\text{helix}} \quad (6)$$

where T_{surface} , $T_{\text{double-bounce}}$, T_{volume} , and T_{helix} represent the expansion matrix of the surface scattering, double-bounce scattering, volume scattering, and helix scattering, respectively. f_s , f_d , f_v , and f_c are the corresponding expansion coefficients, which indicate the specific weights of various types of scattering in total scattering (please see [57] for more details).

Both the Freeman-Durden and Yamaguchi decomposition consider that the volume scattering component comes directly from the cross-polarized term, but topographical change also produces cross-polarized power [58], which leads to an over-estimation of the volume component and negative values for the surface and the double-bounce component, which do not represent a physically possible scattering mechanism. To solve this problem, van Zyl *et al.* [59] decomposition transforms the covariance matrix as follows:

$$C_3 = \begin{bmatrix} \langle |S_{HH}|^2 \rangle & 0 & \langle S_{HH} S_{VV}^* \rangle \\ 0 & \langle 2|S_{HV}|^2 \rangle & 0 \\ \langle S_{VV} S_{HH}^* \rangle & 0 & \langle |S_{VV}|^2 \rangle \end{bmatrix} = a[C_{\text{model}}] + [C_{\text{remainder}}] \quad (7)$$

where matrix $[C_{\text{model}}]$ represents the covariance matrix predicted by a theoretical model. Matrix $[C_{\text{remainder}}]$ is the residual part in the measured matrix $[C_3]$ that is not consistent with the modeled matrix. The value of a must ensure that the eigenvalues of $[C_{\text{remainder}}]$ are positive. Finally, the scattering power is decomposed into three nonnegative components: surface scattering, double-bounce scattering, and volume scattering.

Different from the above scattering decompositions, $H/A/\alpha$ decomposition is based on the statistical property of the decomposition of C and T matrices, which can fully explore different scattering mechanisms [51]. The $H/A/\alpha$ decomposition is also known as the eigen decomposition of the coherency matrix. It analyzes the physical information of the eigen decomposition by three secondary parameters: the

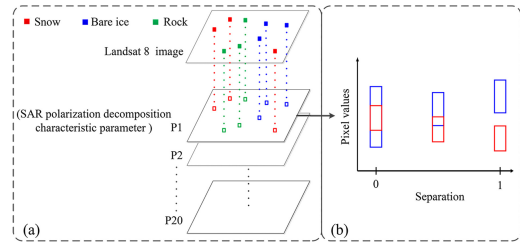


Fig. 3. Schematic of extracting training samples from the object-oriented segmentation optical image and performing PolSAR sample separability calculation. (a) Rectangles of different colors represent various training samples, wherein the solid one represents the training samples selected from the object-oriented segmentation result of optical image, and the open one represents the range in which the training sample is projected into the SAR polarimetric decomposition characteristic parameters. (b) Top and bottom of the red and blue color rectangles represent the maximum and minimum values of snow and bare ice. From left to right, these values become easier to distinguish.

entropy (H), the anisotropy (A), and the mean alpha angle (α). The entropy determines the degree of randomness of the scattering processes, which can also be interpreted as the degree of statistical disorder. The anisotropy represents the relative importance of the second eigenvalue with respect to the third, and it can be employed as a source of discrimination only when $H > 0.7$ because when the entropy is low, there are so many scatterers in the observations, and the second and third eigenvalues are highly affected by noise [60]. The mean alpha angle allows the physical interpretation of the scattering mechanism found by the eigen decomposition. α takes values of 0, $\pi/4$, and $\pi/2$, representing single-bounce scattering, volume scattering, and double-bounce scattering, respectively.

In the preprocessing scheme discussed above, the geocoding of the SAR data and polarimetric decomposition were carried out using the Sentinel Application Platform (SNAP) toolbox, which is an open-source software program of the European Space Agency (ESA).

D. Support Vector Machine Classification

Before the classification of the SAR image, the selection of training samples needs to be combined with the segmentation result of the optical image and the polarimetric decomposition parameter images of SAR data. Fig. 3(a) shows that the multiple pure pixels were selected from the optical image in areas of different surface types corresponding to different glacial zones, and the vector boundaries were derived and superimposed onto the images with the polarimetric decomposition parameters. Seventy percent of the selected pure pixels of each surface type were used to train the classification model, and the rest of the pixels were used for accuracy evaluation, mainly by generating the confusion matrix and the Kappa coefficient.

An SVM classifier is typically a supervised classifier, which requires training samples and distinguishing different types of objects with an optimal hyperplane. It is relatively insensitive to the size of the training samples. The focus is on choosing a kernel function in this process. In this article, the radial basis function (RBF) was selected, and the gamma threshold in the function was set to 0.3. As shown by the flowchart (see Fig. 2) (the blue dashed rectangle), there are three types of input data sets designed for the classification.

- 1) The first data set is a 3–4 band image consisting of the characteristic parameters of each polarimetric decomposition method.
- 2) The second data set is a 4–5 band image formed by adding the local incidence angle image to the 3–4 characteristic parameters of each polarimetric decomposition method.
- 3) The third data set is a multiband image that screens and combines the 20 polarimetric characteristic parameters from the six polarimetric decomposition algorithms. Two methods for parameter screening and combining were designed and are introduced in Section III-E.

There are four categories of land surfaces contained in the images: bare ice representing the glacier ice exposed to air in the ablation zone; snow representing the area covered by the snow in the accumulation zone; rock representing the bare land on the hills surrounding the glaciers and the debris in the terminal moraine or outwash sediment zone; and random scattering for which the pixel value has no physical meaning due to the stretching of the image caused by the terrain.

E. Sample Separation Calculation and Polarimetric Decomposition Parameter Selection Method

Generally, if there is no intersection between any two arrays, the two arrays can be separated. If an inclusion relationship exists between them, they cannot be separated. These rules are applied to the classification as follows [see Fig. 3(b)]: assuming that each characteristic parameter of polarimetric decomposition is a grayscale image layer, polygons of each surface type in the optical image are projected onto the parameter layers. Then, *sample separability*, the degree of separation of two types of training samples in the parameter layers, is defined. All pixel values of the same surface type and in the same layer are grouped into an array A_x^y , where subscript x denotes the characteristic parameter of polarimetric decomposition and superscript y denotes the surface type. Array $A_{x_1}^{y_1}$ contains all the pixel values of type y_1 in the x_1 -polarimetric parameter, while array $A_{x_1}^{y_2}$ contains all pixel values of type y_2 in the x_1 -polarimetric parameter, and so on. If there is no intersection between the two arrays, then the corresponding two surface types can be completely distinguished, and the value of the sample separability is one; if an inclusion relationship exists between the two arrays, the corresponding two types cannot be distinguished, and the value of the sample separability value is zero. If neither of the two above cases is satisfied, the ratio m of the intersected part to the sum of the two arrays is calculated, and the sample separability of the two arrays in the polarimetric decomposition parameter is $(1 - m)$.

We developed two methods for screening and combining the 20 polarimetric characteristic parameters. The first method is based on the sample separability for each surface type. After calculating the separability of all the surface types in the 20 polarimetric characteristic parameters of the polarimetric decompositions, the parameters having the lowest separability are removed. Then, the optimal index factor [61] among those remaining is calculated to further select the polarimetric parameters that are weakly correlated. This process is very similar

to the dimensionality reduction of multispectral data while preserving the information of the original images. Finally, the three parameters with the highest separability for snow, bare ice, and bare land or rocks are selected for combining. This method is called *surface-type-dominated* (STD) combination. The second method considers the scattering mechanisms. The scattering matrix is decomposed into individual scattering mechanisms, such as double-bounce, surface, and volume scattering, and the characteristic parameters with the best separability of any surface types in each scattering mechanism are selected for combining. This method ensures that parameters for the final classification include all the individual scattering mechanisms. We refer to this method as *scattering-mechanism-dominated* (SMD) combination. Comparing the differences between the STD and SMD feature combinations, the former is based on mathematical analysis and the latter is a combination of parameters from physical and mathematical analyses.

IV. RESULTS

A. Sensitivity Analysis

The 20 polarimetric characteristic parameters generated by the six polarimetric algorithms have many similarities in physical meanings and a large amount of redundant information that inevitably leads to strong correlations. Therefore, the sensitivity analysis of the 20 parameters was carried out from three aspects: the degree of sample separation, the parameter correlation coefficient, and the effective data dimension [62], [63]. Let us define a matrix of size $N \times 20$, where the N rows are the number of pixels and the 20 columns are the corresponding 20 characteristic polarimetric parameters. According to the method shown in Fig. 3, the sample separability between any two surface types of snow, bare ice, and bare land/rock for all the characteristic polarimetric parameters is shown in Table I. It can be found that the separability between bare ice and bare land/rock is higher than the separability between the other two types. Further comparisons in each column reveal that the best characteristic parameters of polarimetric decomposition are Freeman_surf, Pauli_b, and $H/A/\alpha_{entropy}$ bands for distinguishing between bare ice and snow; $H/A/\alpha_{alpha}$, $H/A/\alpha_{entropy}$, and Touzi_alpha bands for distinguishing between snow and bare land/rock; and $H/A/\alpha_{entropy}$, Freeman_surf, and $H/A/\alpha_{alpha}$ bands for distinguishing between bare ice and bare land/rock.

A further correlation analysis between pairs of the 20 parameters is shown in Table II, where all correlation coefficients larger than 0.7 have been highlighted. The most independent polarimetric features are from Touzi decomposition, followed by those from $H/A/a$ decomposition. The cross-correlations between the remaining Pauli, Freeman, Yamaguchi, and Van Zyl decomposition parameters are high. Regarding the correlations between the specific polarimetric decomposition parameters, it was found that $H/A/a_{Entropy}$ and $H/A/a_{alpha}$ are only highly correlated with another surface scattering, and the correlation between Freeman_vol and other volume scattering is almost 1.

Finally, we normalized the $N \times 20$ matrix by calculating the mean and variance and then calculating its eigenvalues,

TABLE I
DEGREE OF SAMPLE SEPARATION IN 20 POLARIMETRIC CHARACTERISTIC PARAMETERS

No.	Parameters	Sample Separability		
		Bare ice/Snow	Snow/Rock	Bare ice/Rock
1	Pauli_surf	0.06	0.24	0.42
2	Pauli_vol	0.10	0.26	0.48
3	Pauli_dbl	0.37	0.14	0.24
4	Touzi_psi	0.00	0.15	0.17
5	Touzi_alpha	0.21	0.31	0.49
6	Touzi_phi	0.20	0.26	0.04
7	Touzi_tau	0.00	0.04	0.00
8	Freeman_dbl	0.28	0.08	0.24
9	Freeman_vol	0.13	0.29	0.51
10	Freeman_surf	0.44	0.23	0.56
11	Yamaguchi_dbl	0.14	0.08	0.26
12	Yamaguchi_vol	0.12	0.28	0.50
13	Yamaguchi_surf	0.28	0.25	0.53
14	Yamaguchi_hlx	0.15	0.19	0.27
15	VanZyl_dbl	0.29	0.17	0.15
16	VanZyl_vol	0.13	0.29	0.51
17	VanZyl_surf	0.15	0.29	0.51
18	H/A/a_Entropy	0.35	0.38	0.76
19	H/A/a_Anisotropy	0.08	0.29	0.40
20	H/A/a_alpha	0.28	0.45	0.56

TABLE II
CORRELATION COEFFICIENT OF 20 POLARIMETRIC CHARACTERISTIC PARAMETERS

1	2	3	4	5	6	7	8	9	10	11	12	13	14	15	16	17	18	19	20
1	1	-	-	-	-	-	-	-	-	-	-	-	-	-	-	-	-	-	-
2	0.91	1	-	-	-	-	-	-	-	-	-	-	-	-	-	-	-	-	-
3	0.88	0.89	1	-	-	-	-	-	-	-	-	-	-	-	-	-	-	-	-
4	0.08	0.11	0.08	1	-	-	-	-	-	-	-	-	-	-	-	-	-	-	-
5	-0.17	-0.27	-0.52	-0.02	1	-	-	-	-	-	-	-	-	-	-	-	-	-	-
6	-0.14	-0.14	-0.11	-0.04	-0.03	1	-	-	-	-	-	-	-	-	-	-	-	-	-
7	0.05	0.04	0.03	-0.02	0.01	-0.03	1	-	-	-	-	-	-	-	-	-	-	-	-
8	0.33	0.08	0.23	0.01	-0.02	-0.03	0.03	1	-	-	-	-	-	-	-	-	-	-	-
9	0.93	0.99	0.91	0.11	-0.28	-0.15	0.05	0.10	1	-	-	-	-	-	-	-	-	-	-
10	0.56	0.50	0.77	0.03	-0.68	-0.04	0.00	0.39	0.53	1	-	-	-	-	-	-	-	-	-
11	0.41	-0.15	0.27	0.01	0.04	-0.07	0.02	0.93	0.17	0.36	1	-	-	-	-	-	-	-	-
12	0.91	0.99	0.90	0.10	-0.28	-0.15	0.04	0.08	1.00	0.53	0.15	1	-	-	-	-	-	-	-
13	0.66	0.61	0.84	0.04	-0.66	-0.07	0.00	0.37	0.63	0.95	0.38	0.63	1	-	-	-	-	-	-
14	0.89	0.88	0.85	0.07	-0.29	-0.11	0.06	0.22	0.90	0.56	0.27	0.87	0.66	1	-	-	-	-	-
15	0.95	0.92	0.89	0.12	-0.25	-0.16	0.05	0.29	0.94	0.59	0.36	0.93	0.69	0.89	1	-	-	-	-
16	0.93	0.99	0.91	0.11	-0.28	-0.15	0.05	0.10	1.00	0.53	0.17	1.00	0.63	0.90	0.94	1	-	-	-
17	0.84	0.85	0.94	0.05	-0.54	-0.08	0.04	0.27	0.87	0.77	0.26	0.86	0.81	0.83	0.82	0.87	1	-	-
18	-0.16	-0.12	-0.48	0.03	0.71	-0.09	0.04	-0.17	-0.13	-0.70	-0.15	-0.13	-0.68	-0.18	-0.18	-0.13	-0.46	1	-
19	-0.25	-0.51	-0.34	-0.10	0.23	0.08	0.00	0.44	-0.50	-0.05	0.36	-0.53	-0.13	-0.23	-0.30	-0.50	-0.28	-0.06	1
20	-0.12	-0.18	-0.51	0.00	0.88	-0.02	0.04	-0.10	-0.19	-0.75	-0.04	-0.20	-0.71	-0.19	-0.20	-0.19	-0.51	1.00	0.11

1-20 correspond to the 20 polarization characteristic parameters in Table I, respectively.

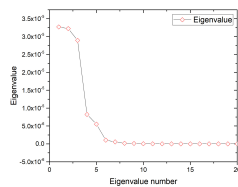


Fig. 4. Eigenvalue of matrix of 20 polarimetric characteristic parameters.

as shown in Fig. 4. The eigenvector can be understood as the direction of the new coordinate axis in the coordinate transformation. The eigenvalue represents the variance of the matrix in the corresponding eigenvector. The larger the eigenvalue, the more information it contains. The results show that such high-dimensional information is transformed and the actual effective information is concentrated in the first five parameters.

Based on the above analysis and according to the rule of using the largest separability and a low redundancy to identify a target, the following characteristic parameters were obtained and used to form the STD combination: $H/A/\alpha_{entropy}$, $H/A/\alpha_{alpha}$, and $Freeman_surf$. On the

TABLE III
MULTIPLE CLASSIFICATION ACCURACY OF THREE GLACIERS IN DIFFERENT POLARIMETRIC DECOMPOSITION

	50197B		Laxia		LBSB	
	without θ^*	with θ	without θ	with θ	without θ	with θ
Pauli	62.42	70.25	74.35	84.24	75.03	91.98
Touzi	59.98	75.88	52.91	70.93	73.11	81.74
Freeman	78.79	86.03	74.76	83.31	87.10	91.37
Yamaguchi	79.00	86.03	74.36	84.02	86.89	91.99
VanZyl	78.07	85.84	75.60	85.69	86.43	91.28
H/A/ α	70.49	81.01	61.89	77.16	84.03	89.84
STD*	76.99	84.60	72.04	83.01	84.07	90.13
SMD*	81.29	86.45	77.25	84.70	88.97	93.78

* θ is local incidence angle

STD (surface type dominated)

SMD (scattering mechanism dominated)

other hand, by comparing the information in each row, we can find the difference in the sample separability between the characteristic parameters from polarimetric decomposition. According to the scattering polarization division, the following polarimetric characteristics can be obtained to form the SMD combination: $Van\ Zyl_dbl$, $Freeman_surf$, and $Freman_vol$.

B. Classification for Each Polarimetric Decomposition

Three classifications in three glacial zones were performed. Table III shows the overall accuracy in identifying the three glaciers based on the various decomposition parameters. The overall accuracy ranges from 52.6% to 87.0% and the classification of polarimetric decomposition parameters based on the decomposition of the covariance matrix is very accurate. The $Freeman_Durden$, $Yamaguchi$, and $Van\ Zyl$ decompositions achieve the highest overall accuracy, all exceeding 75.0%. In a comparison among the three glaciers, the $LBSB$ glacier has the highest overall average accuracy [82.10%, Fig. 5(c1)], followed by the 50197B glacier [71.46%, Fig. 5(a1)] and the $Laxia$ glacier [68.98%, Fig. 5(b1)]. After the local incidence angle was taken as a single band and combined with the characteristic polarimetric decomposition parameter bands to form a multiband image for extracting the classification training samples, the highest precision for the three glaciers increased to 91.98% (see Table III), demonstrating that the inclusion of local incidence angle to the suite of classifiers improves the classification accuracy and effectively reduces the fragmentation of the classification results.

By comparing the confusion matrices, we found that snow was identified with the highest accuracy in the classification based on the single-polarimetric decomposition parameter, followed by bare land (or rocks) and bare ice. After adding the local incidence angle to the suite of classifiers, a large portion of the bare ice that was misclassified as rocks was corrected, but it also caused an increase in the omission errors from classifying snow as rocks or vice versa in the classification based on the decomposition parameters of partial polarization.

C. Classification After Combining Polarimetric Decomposition Parameters

Two feature combination methods were adopted after screening the 20 polarimetric characteristic parameters. The

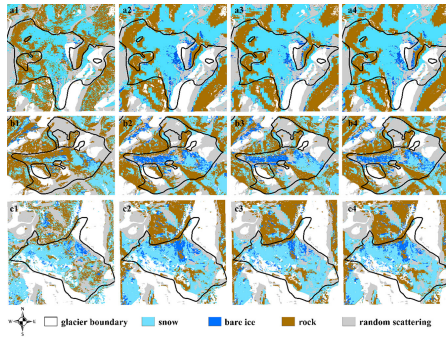


Fig. 5. Classified images using the SVM technique. Each row is for the same glacier, and each column is under the same classification condition. (a)–(c) correspond to the 50197B glacier, Laxia glacier, and LBSB glacier (shown in Fig. 1), respectively. 1 represents the most accurate classification based on the parameter of individual polarimetric decomposition. 2 represents the same condition as 1 but with the local incident angle considered. 3 represents results from the STD combination method. 4 represents results from the SMD combination method. Among them, (a1)–(c1) correspond to the classified results based on parameters of Yamaguchi, Van Zyl, and Freeman-Durden decompositions, respectively. The black solid line is the glacier boundary from the second glacier inventory data set of China.

first is the STD combination, based on the mathematical analysis of the 20 parameters, which selects three parameters with the largest degree of separation and less cross correlation. It is clear from Table III that the overall accuracy of the STD combination is 84.07% (LBSB glacier) and it can reach 90.13% after being combined with the local incidence angle [see Fig. 5(c3)], but it cannot exceed the classification accuracy based on the single decomposition (Freeman, Yamaguchi and Van Zyl) parameters.

The second combination method (SMD) is based on the simple scattering mechanism. From the 20 polarimetric characteristic parameters, the surface scattering, volume scattering, and the double-bounces scattering characteristics with the largest degree of separation and less cross correlation were selected. The results show that after the SMD combination, the highest classification accuracy reached 88.97% for the LBSB glacier, and the classification accuracy of each glacier after combining exceeded the classification accuracy of the single-polarimetric decomposition parameter, reaching 93.78% after taking into account the local incidence angle [see Fig. 5(c4)].

It seems that the feature combination method combined with the simple scattering mechanism can improve the recognition accuracy of the glacial area. This finding also shows that the polarimetric decomposition parameters can provide more physical parameters of the glacier surface, and the simple scattering mechanism based on the model decomposition can improve glacier identification.

V. DISCUSSION

The results from Section IV show that the classification accuracies of a glacier vary greatly with different polarimetric decomposition parameters. Accordingly, the classification accuracies of the same polarimetric decomposition parameter applied to different glacial regions are also different. In this regard, we analyzed the influencing factors in the process of

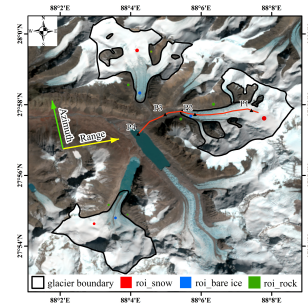


Fig. 6. True color composite of Landsat 8 OLI image of the Laxia glacier. The red line is a downslope profile along the glacier. The black solid triangle P1–P4 denote snow, bare ice, bare land/rock, and water in the lake, respectively. “roi” denotes the region of interest. The small red dots represent the snow samples, located in the accumulation zone; the blue dots represent the bare ice samples, located in the glacier tongue and which is mainly glacier ice; and the green dots represent the bare land/rock samples, located on both sides of the glaciers. The black polygons represent the boundary of the three glaciers. The green and yellow arrows indicate the azimuth and range direction of the imaging radar system, respectively. The range direction is the direction of radar beam propagation.

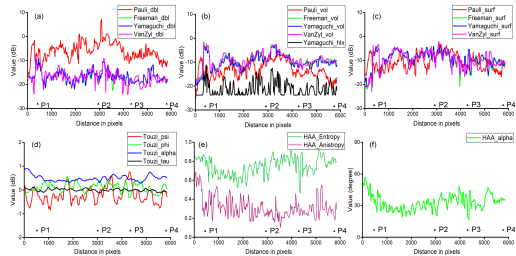


Fig. 7. Spatial distributions of the parameter values of different polarimetric decompositions along the downslope profile from the snow accumulation zone to the lake area shown in Fig. 6. (a)–(c) All the double-bounce scattering, volume scattering, and surface scattering from Pauli, Freeman, Yamaguchi, and Van Zyl decompositions, respectively. (d) Value of polarimetric parameters from Touzi decomposition. (e) and (f) Values of entropy anisotropy and α , respectively.

glacier identification from two aspects: characteristic polarimetric parameters and topography.

A. Effect of Different Characteristic Polarimetric Parameters on Classification

The accuracy of classification sometimes depends largely on the training samples. Therefore, we chose the Laxia glacier, which has the largest variance in the classification accuracy, as an example to analyze the differences and causes of the glacier identification accuracy of various polarimetric decompositions. As shown in Fig. 6, points P1, P2, P3, and P4 are located in the accumulation zone, the ablation zone, the terminal moraine or outwash sediment zone, and the ice-marginal lake zone, respectively. The corresponding land types are snow, bare ice, bare land/rock, and water. We obtained the values of all the characteristic polarimetric parameters along the downslope profile in the middle of the Laxia glacier and generated curves (see Fig. 7) and 3-D scatterplots (see Fig. 8).

Since the Pauli, Freeman, Yamaguchi, and Van Zyl decompositions perform the decomposition process with the same three basic scattering mechanisms, let us compare the results from these decompositions. The curves shown in Fig. 7 reveal that the double-bounce scattering, volume scattering, and the

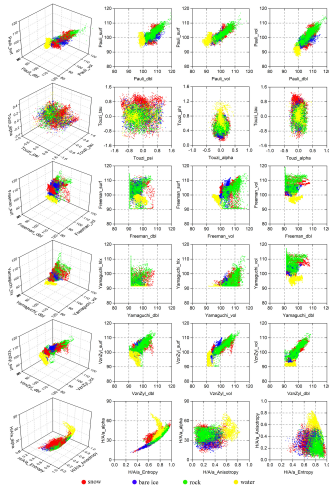


Fig. 8. Distributions of the 20 polarimetric characteristic parameters for snow, bare ice, rock, and water surface types. Rows from the top to the bottom represent the Pauli, Touzi, Freeman, Yamaguchi, Van Zyl, and $H/A/\alpha$ decomposition method, respectively. Columns from left to right are the 3-D scatterplots of the values of polarimetric parameters from each decomposition method in the polarimetric feature space, projected 2-D scatter plots of the 3-D scatterplots on the planes as indicated by the axis titles.

surface scattering have similar shapes and have the following characteristics: the double-bounce scattering curve has three distinct peaks. These peaks appear in the middle of the transition zone between each of the two types of land surfaces, namely, near the snow line, the end of the ice tongue, and the edge of the lake. The volume scattering curve starts to increase from the snow zone. After some fluctuations, it reaches a peak at the ice tongue and then gradually decreases. Finally, after a peak at the edge of the lake, it drops to a stable value of approximately -15 dB. For the surface scattering curves, the overall distribution is approximately -10 dB, which is stable in the bare ice zone, and valleys appear at only the ice tongue and the lake. Different from these curves, the curves of the four polarimetric characteristics from Touzi decomposition in the glacial area have no obvious variation pattern. Unlike these four decompositions, the $H/A/\alpha$ decomposition method is based on the statistics of the scattering matrix. The curves represent the change in entropy, anisotropy, and alpha. They show that the entropy and anisotropy seem to have a symmetrical trend centered on the X-axis. Although the values of entropy and alpha are not the same, they have a similar shape: the entropy and alpha curves reach a peak at the end of the ice tongue and the lake, while the anisotropy curve reaches a valley at the corresponding position.

The changes in these curves indicate that the values of the characteristic polarimetric parameters depend on land surface types. We computed the 20 polarimetric characteristic parameters for all the land type samples and presented them in the form of the scatterplots, as shown in Fig. 8. Each row represents a polarimetric decomposition method. The 3-D scatterplots in the leftmost column represent the values of the respective parameters for all four land surface types. The 2-D scatterplots from left to right in each row are the projected 2-D plots of the 3-D scatterplots on the corresponding planes as indicated by the axis titles.

The high-altitude accumulation zone is covered with the snow, ranging from new snow at the surface to old and metamorphosed snow at deeper levels. Radar backscattering from the snow accumulation zone generally includes both surface scattering and volume scattering. According to the scatterplots, the backscattering due to the single type of land surface is dominated by dipole scattering and belongs to the medium entropy multiple scattering [64]. As the altitude decreases (between P1 and P2), the snow depth decreases along the downslope profile, and the backscattered signals received not only from the snow layer but also from the underlying ice surface, which is stronger than those from the snow. Even if the surface snow layer melts and eventually disappears (from P2 to P3), the radar beam can penetrate into the glacial ice, the presence of crystals inside the glacier ice and the crevasses cause an increase in the volume scattering. At the same time, a decrease in the smoothness causes a reduction in the anisotropy [65]. In the low-altitude zone of the ice tongue, the squeezing of ice caused by the downward movement of glacier ice forms wrinkles. When a radar beam touches these pleats, it returns due to the double-bounce scattering. Eventually, the roughness of the terminal moraine at the end of the ice tongue and the surface tills creates a strong backscattering peak between points P2 and P3. Due to the decrease in roughness as we transverse from P3 to P4, the double-bounce scattering component of the terminal moraine or outwash sediment zone (P3) gradually decreases and remains stable, and the surface scattering component increases. In the lake zone (around P4), an increase in the dielectric constant due to more soil moisture generates a significant backscatter peak. Eventually, at the edge of the lake, the topographical changes cause a higher double-bounce component and alpha value. In the lake zone, the specular reflection of radar beams by the lake water causes the radar backscattering to plummet and remain low. According to the scatterplot, the backscattering in the lake zone belongs to medium entropy but includes surface and dipole scattering.

The surface type affects the value of the polarimetric parameters, and the physicochemical properties of the land surface are the underlying causes. Therefore, we screened and combined these parameters based on the type of surface (STD). From the classification accuracy table, we found that several classification schemes with the highest accuracy were based on simple scattering mechanisms. Therefore, we reorganized the polarimetric parameters according to the scattering mechanism (SMD). This combination is similar to selecting the parameters corresponding to the largest eigenvalues and reprojecting them into the same coordinate system according to the corresponding eigenvectors. Fig. 9 shows the scatterplots of the polarimetric parameters in the polarimetric feature space after the STD and SMD combination schemes. Compared to the STD combination scheme, the SMD combination scheme increases the degree of separation of snow, bare ice, and rock. These results demonstrate the advantages of using the polarimetric parameter combination method proposed in this article to improve the separability of different land surface classes.

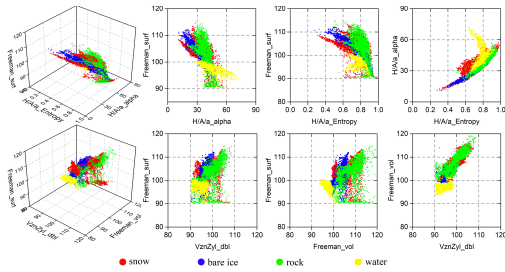


Fig. 9. Distributions of characteristic polarimetric parameters of all samples in the feature space after the STD combination (top row) and the SMD combination (second row). Columns from left to right are the 3-D scatterplots of the values of polarimetric parameters in the polarization feature space, projected 2-D scatterplots of the 3-D scatterplots on the planes as indicated by the axis titles. Each point is associated with one pixel of the sample, different colors indicate different land types.

B. Effect of Topographic Factors on Classification

From the above analysis, we can see that the polarimetric characteristics can affect the classification accuracy, but radar backscattering strongly depends on the local incidence angle [66], which is a function of the slope and aspect of the surface. The local incidence angle also affects the polarization and scattering direction, resulting in changes in the radar polarimetric characteristics [67]–[69]. However, the difference in slope among the glaciers in the study area is small, and the largest difference in the local incidence angle is caused by the aspect. Therefore, a parameter, β , is defined to analyze how the aspect affects the classification accuracy by changing the polarimetric characteristics. β is the angle between the surface aspect and the direction of the radar beam propagation, and its value ranges from 0° to 180° . Fig. 6 shows the spatial relationship between the direction of the glacier and the direction of operation of the radar sensor. The β values of the three glaciers are as follows: 46° for the LBSB glacier, 107° for the 50197B glacier, and 162° for the Laxia glacier. After choosing three land types in the glacier zone (i.e., snow, bare ice, and bare land/rocks, where rocks were selected on either side of the glacier), the spatial distribution of the samples is shown in Fig. 6. As Yamaguchi polarimetric decomposition shows the largest difference among the three glaciers, we used it as an example to analyze the impact of the terrain.

Fig. 10 shows the radar intensity scatterplots for the various polarimetric parameters of snow, bare ice, and bare land/rocks in dihedral scattering (dbl), surface scattering (surf), volume scattering (vol), and helix scattering (hlx) versus the β angle. For the LBSB glacier (left column in Fig. 10), the β angle is distributed within 0° – 120° in the snow area, within 0° – 180° in the bare ice area, and clearly concentrated within 15° – 150° in the bare land/rock area. In terms of the values of the polarimetric parameters, both snow and bare ice are less than 0, and the value of bare ice is higher than that of snow, which is most obvious in surface scattering [see Fig. 10(d)] and volume scattering [see Fig. 10(g)]. The polarimetric parameter value of rock increases with increasing β . When β exceeds 120° , the surface and volume scattering values exceed 0. For the 50197B glacier (middle column of Fig. 10), the β angle is within 0° – 180° in the snow area while the angle is mainly within 60° – 180°

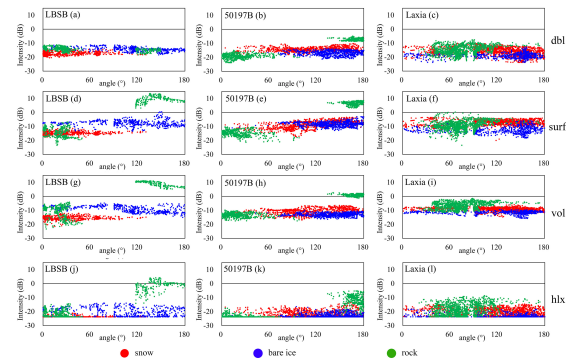


Fig. 10. Scatter plots of radar intensity of the polarimetric parameter versus aspect (β angle) for the surfaces of snow, glacier ice, and bare land/rock of each of the three glaciers. The x-axis is the β angle, and the y-axis is the value of the polarimetric characteristic parameters in dB. The red points represent the samples of snow, blue points represent the samples of bare ice, and green points represent the samples of bare land or rock, respectively. Each column is for the same glacier. Each row corresponds to a polarimetric parameter: the first row from the top is for the double-bounce scattering, the second row is for the surface scattering, the third row is for volume scattering, and the bottom row is for helix scattering.

in the bare ice zone. In the bare land/rock zone, the β angle values are mainly distributed within two intervals: 0° – 60° and 150° – 180° . It is worth noting that for the 50197B glacier, the polarimetric characteristic values of snow are generally higher than those of bare ice, and the polarimetric parameter values of bare land/rock are lower than those of the LBSB glacier. However, the increasing trend in the polarimetric parameters of snow, bare ice, and bare land/rock with increasing β has not changed. For the Laxia glacier (right column of Fig. 10), the β angle distribution of snow and bare ice is similar, ranging within 0° – 180° , and the β angles of bare land/rock are between 40° and 180° . All the polarimetric parameter values of different land types do not change significantly with the increase in the β angle, and they are distributed within -25 – 0 dB, making them indistinguishable.

Comparing each column in Fig. 10 can reveal the effect of aspect on the polarimetric parameters. When the β angle of the glacier is small [see Fig. 10(a), (d), (g), and (j)], the polarimetric parameter values of snow are smaller than those of bare ice, and there is a clear boundary between them. However, the bare land/rock is mostly affected by the aspect. Half of the bare land/rocks face away from the direction of the radar beam and the other half face toward the radar beam. The former leads to foreshortening, and the latter strongly reflects the radar signal. This behavior leads to a significant increase in the polarimetric parameter values with increasing β , despite the discrete distribution of β angles, so that a part of the bare land/rock can be well recognized. As the β angle of the glacier increases [see Fig. 10(b), (e), (h), and (k)], the characteristic values of the accumulation zone exceed those of the ablation zone, and the boundary between the two zones becomes blurred. The rock area is still only partially recognized. When the β angle of the glacier exceeds a certain threshold, the characteristic value of snow is higher than that of bare ice, and these two values no longer show an increasing trend with increasing β . When the glacier is parallel to the direction of the radar beam, the bare land/rocks on

both sides of the glacier can be illuminated by the radar beam. Thus, the distribution of β values of bare land/rock is no longer concentrated in two separate intervals, as shown in Fig. 10(c), (f), (i), and (l). This phenomenon makes all the polarimetric parameter values of bare land/rock overlap with those of snow and bare ice, and the three become indistinguishable.

As the β angle increases, the polarimetric characteristics of bare ice tend to be stable, and the polarimetric characteristics of snow continue to increase slightly, while the scattering characteristics of the rocks vary greatly. Thus, the recognizability of rocks is reduced, increasing the possibility of classifying rocks as glacier ice. Therefore, the influence of aspect on glacial identification is mainly reflected in the influence of rock identification.

VI. CONCLUSION

In summary, the preprocessing and target polarimetric decomposition of the fully polarized radar data were carried out. A high-resolution Landsat 8 OLI optical image was segmented by object orientation, and the training samples were extracted for SVM-based classification. The classification was performed on three data sources: the characteristic polarimetric parameters of each polarimetric decomposition method, the characteristic parameters of each polarimetric decomposition method while taking into account the local incidence angle, and the optimal polarimetric characteristic parameters that were selected and combined using two combination methods after all 20 polarimetric characteristic parameters of the polarimetric decompositions were screened. By comparing the accuracy of the two combination methods in the identification of three glaciers, the polarimetric characteristics of alpine glaciers and the influence of terrain on glacial identification were analyzed.

The results classified using SVM show that the highest classification accuracy based on single polarimetric parameters was 87.1%, but it increased to 91.98% after adding the local incidence angle to the suite of classifiers. Comparing the confusion matrices, the addition of the local incidence angle can increase the commission errors between bare ice and rocks but improve the overall classification accuracy of glaciers.

The results also show that the aspect of a glacier surface is an important factor affecting the identification of alpine glaciers. It not only impacts the amplitude of the backscattered signal but also changes the polarimetric characteristics of an object and thus can impact the classification accuracy. Bare land/rocks are more affected by the slope, followed by snow. Bare glacial ice is the least affected by the terrain due to its relatively smooth surface. Based on the above information, the effect of the STD polarimetric parameter combination on improving classification accuracy is not obvious. The incoherent polarimetric decomposition based on the covariance matrix decomposes the scatter signal into dihedral scattering (dbl), surface scattering (surf) and volume scattering (vol) parameters, which is an effective tool for isolating individual scattering mechanisms of snow and bare land/rock. Therefore, the classification accuracy of the

SMD combination method reaches 88.97%, which exceeds the classification accuracy of arbitrary single-polarimetric decomposition parameters. It reaches 93.78% after considering the local incidence angle. The study shows that high-resolution optical data used for selecting training samples and an appropriate combination of characteristic parameters for the SAR polarimetric decompositions can be employed for effective alpine glacier identification and monitoring.

ACKNOWLEDGMENT

The Landsat data used are obtained from the Google Earth Engine platform (<https://earthengine.google.com/>). The authors would like to thank the Cold and Arid Regions Science Data Center for free provision of the Second Glacier Inventory data set of China (V 1.0).

REFERENCES

- [1] W. W. Immerzeel, L. P. H. van Beek, and M. F. P. Bierkens, "Climate change will affect the Asian water towers," *Science*, vol. 328, no. 5984, pp. 1382–1385, Jun. 2010.
- [2] T. Yao *et al.*, "Different glacier status with atmospheric circulations in Tibetan Plateau and surroundings," *Nature Climate Change*, vol. 2, no. 9, pp. 663–667, 2012.
- [3] M. Jefferson, "IPCC fifth assessment synthesis report: 'Climate change 2014: Longer report': Critical analysis," *Technol. Forecasting Social Change*, vol. 92, no. 1, pp. 362–363, Mar. 2015.
- [4] Y. Nie, Y.-L. Zhang, L.-S. Liu, and J.-P. Zhang, "Monitoring glacier change based on remote sensing in the Mt. Qomolangma national nature preserve, 1976–2006," (in Chinese), *Acta Geographica Sinica*, vol. 65, no. 1, pp. 13–28, Jan. 2010.
- [5] D. Scherler, B. Bookhagen, and M. R. Strecker, "Spatially variable response of Himalayan glaciers to climate change affected by debris cover," *Nature Geosci.*, vol. 4, pp. 156–159, Jan. 2011.
- [6] C. Harris *et al.*, "Permafrost and climate in Europe: Monitoring and modelling thermal, geomorphological and geotechnical responses," *Earth Sci. Rev.*, vol. 92, nos. 3–4, pp. 117–171, Feb. 2009.
- [7] F. Paul *et al.*, "The glaciers climate change initiative: Methods for creating glacier area, elevation change and velocity products," *Remote Sens. Environ.*, vol. 162, pp. 408–426, Jun. 2015.
- [8] N. K. Agarwal, "Terrestrial photogrammetric mapping of the Neh-Nar glacier in Himalaya, India," *ISPRS J. Photogramm.*, vol. 44, no. 4, pp. 245–252, Dec. 1989.
- [9] B. Song *et al.*, "Identifying automatically the debris-covered glaciers in China's monsoonal temperate-glacier regions based on remote sensing and GIS," (in Chinese), *J. Glaciol. Geocryol.*, vol. 29, no. 3, pp. 456–462, Jun. 2007.
- [10] T. Bolch, B. Menounos, and R. Wheate, "Landsat-based inventory of glaciers in western Canada, 1985–2005," *Remote Sens. Environ.*, vol. 114, no. 1, pp. 127–137, Jan. 2010.
- [11] T. Bolch *et al.*, "The state and fate of Himalayan glaciers," *Science*, vol. 336, no. 6079, pp. 310–314, Apr. 2012.
- [12] W. T. Pfeffer *et al.*, "The Randolph glacier inventory: A globally complete inventory of glaciers," *J. Glaciol.*, vol. 60, no. 221, pp. 537–552, Jun. 2017.
- [13] S. Y. Liu *et al.*, "The contemporary glaciers in China based on the Second Chinese Glacier Inventory," *Acta Geographica Sinica*, vol. 70, no. 1, pp. 3–16, 2015.
- [14] L. Liu *et al.*, "Morphometric controls on glacier mass balance of the Puruogangri ice field, central Tibetan Plateau," *Water*, vol. 8, no. 11, p. 496, Nov. 2016.
- [15] P. Rastner, T. Strozzi, and F. Paul, "Fusion of multi-source satellite data and DEMs to create a new glacier inventory for Novaya Zemlya," *Remote Sens.*, vol. 9, no. 11, p. 1122, Nov. 2017.
- [16] K. Liu, N. Wang, and X. Bai, "Variation of glaciers in the Nubra basin, Karakoram Mountains, revealed by remote sensing images during 1993–2015," (in Chinese), *J. Glaciol. Geocryol.*, vol. 39, no. 4, pp. 710–719, Aug. 2017.
- [17] Q. Zhang and G. Zhang, "Glacier elevation changes in the western Nyainqentanglha range of the Tibetan plateau as observed by TerraSAR-X/Tandem-X images," *Remote Sens. Lett.*, vol. 8, no. 12, pp. 1142–1151, Aug. 2017.

- [18] J. Zhou, Z. Li, and X. Li, "A comparative study of coherence patterns of C-band and L-band interferometric SAR in western glacier areas," (in Chinese), *Remote Sens. Land Resour.*, vol. 21, no. 2, pp. 9–13, Jun. 2009.
- [19] J. A. Richards, "Scattering from earth surface features," in *Remote Sensing With Imaging Radar: Signals and Communication Technology*, 1st ed. Berlin, Germany: Springer, 2009, pp. 25–26. [Online]. Available: <https://www.springer.com/us/book/9783642020193>
- [20] M. Callegari *et al.*, "A Pol-SAR analysis for alpine glacier classification and snowline altitude retrieval," *IEEE J. Sel. Topics Appl. Earth Observ. Remote Sens.*, vol. 9, no. 7, pp. 3106–3121, Jul. 2016.
- [21] H. Rott and C. Mätzler, "Possibilities and limits of synthetic aperture radar for snow and glacier surveying," *Ann. Glaciol.*, vol. 9, pp. 195–199, Jan. 1987.
- [22] J. C. Shi and J. Dozier, "Measurements of snow-covered and glacier-covered areas with single-polarization SAR," in *Proc. Int. Symp. Remote Sens. Snow Ice*, Boulder, CO, USA, 1992, vol. 17, no. 17, pp. 72–76.
- [23] S. Adam, A. Pietroniro, and M. M. Brugman, "Glacier snow line mapping using ERS-1 SAR imagery," *Remote Sens. Environ.*, vol. 61, no. 1, pp. 46–54, Jul. 1997.
- [24] T. Strozzi, A. Wiesmann, A. Kääb, S. Joshi, and P. Mool, "Glacial lake mapping with very high resolution satellite SAR data," *Natural Hazards Earth Syst. Sci.*, vol. 12, no. 8, pp. 2487–2498, Aug. 2012.
- [25] G. Singh, G. Venkataraman, Y. Yamaguchi, and S.-E. Park, "Capability assessment of fully polarimetric ALOS-PALSAR data for discriminating wet snow from other scattering types in mountainous regions," *IEEE Trans. Geosci. Remote Sens.*, vol. 52, no. 2, pp. 1177–1196, Feb. 2014.
- [26] M. König, J. G. Winther, and E. Isaksson, "Measuring snow and glacier ice properties from satellite," *Rev. Geophys.*, vol. 39, no. 1, pp. 1–28, Feb. 2001.
- [27] L. Huang, B.-S. Tian, Q. Chen, and J.-M. Zhou, "Monitoring glacier zones and snow/firn line changes in the Qinghai-Tibetan Plateau using C-band SAR imagery," *Remote Sens. Environ.*, vol. 137, no. 10, pp. 17–30, Oct. 2013.
- [28] L. Huang, Z. Li, B.-S. Tian, Q. Chen, J.-L. Liu, and R. Zhang, "Classification and snow line detection for glacial areas using the polarimetric SAR image," *Remote Sens. Environ.*, vol. 115, no. 7, pp. 1721–1732, Jul. 2011.
- [29] W. H. Peake and T. L. Oliver, "The response of terrestrial surfaces at microwave frequencies," Ohio State Univ. Electrosci. Lab., Columbus, OH, USA, Tech. Rep. AFAL-TR-70-301, 1971. [Online]. Available: <https://apps.dtic.mil/dtic/tr/fulltext/u2/884106.pdf>
- [30] S. Kundu and M. Chakraborty, "Delineation of glacial zones of Gangotri and other glaciers of central Himalaya using RISAT-1 C-band dual-pol SAR," *Int. J. Remote Sens.*, vol. 36, no. 6, pp. 1529–1550, Mar. 2015.
- [31] R. M. Goldstein, H. Engelhardt, B. Kamb, and R. M. Frolich, "Satellite radar interferometry for monitoring ice sheet motion: Application to an antarctic ice stream," *Science*, vol. 262, no. 5139, pp. 1525–1530, 1993.
- [32] L. Y. Li, "Study on variation and mass balance estimations of glacier in Yigong Zangbu basin, Tibet by using multi-source remote sensing data," Ph.D. dissertation, Dept. Geographic Inf. Syst., Nanjing Univ., Nanjing, China, 2018.
- [33] V. Kumar, Y. Larsen, and Y. Larsen, "Estimation and validation of glacier surface motion in the northwestern Himalayas using high-resolution SAR intensity tracking," *Int. J. Remote Sens.*, vol. 34, no. 15, pp. 5518–5529, Apr. 2013.
- [34] J. J. Sharma, I. Hajnsek, K. P. Papathanassiou, and A. Moreira, "Polarimetric decomposition over glacier ice using long-wavelength airborne PolSAR," *IEEE Trans. Geosci. Remote Sens.*, vol. 49, no. 1, pp. 519–535, Jan. 2011.
- [35] P. K. Thakur *et al.*, "Estimation of snow cover area, snow physical properties and glacier classification in parts of western Himalayas using C-band SAR data," *J. Indian Soc. Remote*, vol. 45, pp. 525–539, Jul. 2016.
- [36] G. Parrella, I. Hajnsek, and K. P. Papathanassiou, "Polarimetric decomposition of L-band PolSAR backscattering over the Austfonna ice cap," *IEEE Trans. Geosci. Remote Sens.*, vol. 54, no. 3, pp. 1267–1281, Mar. 2016.
- [37] L. Huang, Z. Li, B.-S. Tian, J.-M. Zhou, and Q. Chen, "Recognition of supraglacial debris in the Tianshan mountains on polarimetric SAR images," *Remote Sens. Environ.*, vol. 145, no. 5, pp. 47–54, Apr. 2014.
- [38] F. Paul *et al.*, "Error sources and guidelines for quality assessment of glacier area, elevation change, and velocity products derived from satellite data in the Glaciers_cci project," *Remote Sens. Environ.*, vol. 203, no. 15, pp. 256–275, Dec. 2017.
- [39] S. R. Cloude, "Depolarisation in surface and volume scattering," in *Polarization: Applications in Remote Sensing*, 1st ed. Oxford, U.K.: Oxford Univ. Press, 2010, p. 123. [Online]. Available: <https://global.oup.com/academic/product/polarisation-applications-in-remote-sensing-9780199569731?q=Polarisation:%20Applications%20in%20Remote%20Sensing.&lang=en&cc=en>
- [40] N. Usami, A. Muhuri, A. Bhattacharya, and A. Hirose, "PolSAR wet snow mapping with incidence angle information," *IEEE Geosci. Remote Sens. Lett.*, vol. 13, no. 12, pp. 2029–2033, Dec. 2016.
- [41] J. Panthi *et al.*, "Spatial and temporal variability of rainfall in the Gandaki river basin of Nepal Himalaya," *Climate*, vol. 3, no. 1, pp. 210–226, Mar. 2015.
- [42] M. Ménégoz, H. Gallée, and H. W. Jacobi, "Precipitation and snow cover in the Himalaya: From reanalysis to regional climate simulations," *Hydrol. Earth Syst. Sci.*, vol. 17, pp. 3921–3936, Oct. 2013.
- [43] S. Y. Liu *et al.*, "The second glacier inventory dataset of China (version 1.0)," Cold Arid Regions Sci. Data Center Lanzhou, Lanzhou, China, Tech. Rep., 2014.
- [44] A. Grinsted, "An estimate of global glacier volume," *Cryosphere*, vol. 7, pp. 141–151, Jan. 2013.
- [45] V. Radic and R. Hock, "Regional and global volumes of glaciers derived from statistical upscaling of glacier inventory data," *J. Geophys. Res. Earth*, vol. 115, Mar. 2010, Art. no. F01010.
- [46] L. Shiyin, S. Wenxin, S. Yongping, and L. Gang, "Glacier changes since the little ice age maximum in the western Qilian Shan, northwest China, and consequences of glacier runoff for water supply," *J. Glaciol.*, vol. 49, no. 164, pp. 117–124, Jan. 2003.
- [47] H. Frey, F. Paul, and T. Strozzi, "Compilation of a glacier inventory for the western Himalayas from satellite data: Methods, challenges, and results," *Remote Sens. Environ.*, vol. 124, pp. 832–843, Sep. 2012.
- [48] S. R. Cloude, "Target decomposition theorems in radar scattering," *Electron. Lett.*, vol. 21, no. 1, pp. 22–24, Jan. 1985.
- [49] S. R. Cloude, "Group theory and polarization algebra," *OPTIK*, vol. 75, no. 1, pp. 26–36, Dec. 1986.
- [50] J.-S. Lee, J.-H. Wen, T. L. Ainsworth, K.-S. Chen, and A. J. Chen, "Improved sigma filter for speckle filtering of SAR imagery," *IEEE Trans. Geosci. Remote Sens.*, vol. 47, no. 1, pp. 202–213, Jan. 2009.
- [51] S. R. Cloude and E. Pottier, "A review of target decomposition theorems in radar polarimetry," *IEEE Trans. Geosci. Remote Sens.*, vol. 34, no. 2, pp. 498–518, Mar. 1996.
- [52] B. M. Minchew, "Polarimetric SAR decomposition of temperate ice cap Hofsjökull, central Iceland," M.S. thesis, Dept. Aerosp. Eng. Mech., Univ. Texas Austin, Austin, TX, USA, 2010.
- [53] R. Touzi, A. Deschamps, A. M. Demers, and G. Rother, "The Touzi decomposition for wetland classification using polarimetric C-band SAR," in *Proc. 4th Int. Workshop Sci. Appl. SAR Polarimetry Polarimetric Interferometry (PolInSAR)*, Frascati, Italy, Jan. 2009, p. 261.
- [54] R. Touzi, "Target scattering decomposition in terms of roll-invariant target parameters," *IEEE Trans. Geosci. Remote Sens.*, vol. 45, no. 1, pp. 73–84, Jan. 2007.
- [55] A. Freeman and S. L. Durden, "A three component scattering model for polarimetric SAR data," *IEEE Trans. Geosci. Remote Sens.*, vol. 36, no. 3, pp. 963–973, May 1998.
- [56] Y. Yamaguchi, T. Moriyama, M. Ishido, and H. Yamada, "Four-component scattering model for polarimetric SAR image decomposition," *IEEE Trans. Geosci. Remote Sens.*, vol. 43, no. 8, pp. 1699–1706, Aug. 2005.
- [57] Y. Yajima, Y. Yamaguchi, R. Sato, H. Yamada, and W. M. Boerner, "POLSAR image analysis of wetlands using a modified four-component scattering power decomposition," *IEEE Trans. Geosci. Remote Sens.*, vol. 46, no. 6, pp. 1667–1673, Jun. 2008.
- [58] J. Lee and E. Pottier, "Pol-InSAR forest mapping and classification," in *Polarimetric Radar Imaging: From Basics to Applications*, 1st ed. Boca Raton, FL, USA: CRC Press, 2009, p. 314. [Online]. Available: <https://www.crcpress.com/Polarimetric-Radar-Imaging-From-Basics-to-Applications/Lee-Pottier/p/book/9781420054972>
- [59] J. J. van Zyl, M. Arii, and Y. Kim, "Model-based decomposition of polarimetric SAR covariance matrices constrained for nonnegative eigenvalues," *IEEE Trans. Geosci. Remote Sens.*, vol. 49, no. 9, pp. 3452–3459, Sep. 2011.

- [60] J. Lee and E. Pottier, "H/A/ α polarimetric decomposition theorem," in *Polarimetric Radar Imaging: From Basics to Applications*, 1st ed. Boca Raton, FL, USA: CRC Press, 2009, p. 236. [Online]. Available: <https://www.crcpress.com/Polarimetric-Radar-Imaging-From-Basics-to-Applications/Lee-Pottier/p/book/9781420054972>
- [61] P. Chavez, G. Berlin, and L. Sowers, "Statistical method for selecting Landsat MSS ratios," *J. Appl. Photographic Eng.*, vol. 8, no. 1, pp. 23–30, Jan. 1984.
- [62] A. Villa, L. Iannini, D. Giudici, A. Monti-Guarnieri, and S. Tebaldini, "Calibration of SAR polarimetric images by means of a covariance matching approach," *IEEE Trans. Geosci. Remote Sens.*, vol. 53, no. 2, pp. 674–686, Feb. 2015.
- [63] S. Tebaldini, F. Rocca, M. M. d'Alessandro, and L. Ferro-Famil, "Phase calibration of airborne tomographic SAR data via phase center double localization," *IEEE Trans. Geosci. Remote Sens.*, vol. 54, no. 3, pp. 1775–1792, Mar. 2016.
- [64] K. Ji and Y. Wu, "Scattering mechanism extraction by a modified Cloude-Pottier decomposition for dual polarization SAR," *Remote Sens.*, vol. 7, no. 6, pp. 7447–7470, 2015.
- [65] J. Lee and E. Pottier, "Selected polarimetric SAR application," in *Polarimetric Radar Imaging: From Basics to Applications*, 1st ed. Boca Raton, FL, USA: CRC Press, 2009, p. 346. [Online]. Available: <https://www.crcpress.com/Polarimetric-Radar-Imaging-From-Basics-to-Applications/Lee-Pottier/p/book/9781420054972>
- [66] H. Rott and T. Nagler, "Monitoring temporal dynamics of snowmelt with ERS-1 SAR," in *Proc. Int. Geosci. Remote Sens. Symp. Quant. Remote Sens. Sci. Appl. (IGARSS)*, Firenze, Italy, vol. 3, Jul. 1995, pp. 1747–1749.
- [67] B. Souissi and M. Ouarzeddine, "Analysis of orientation angle shifts on the polarimetric data using Radarsat2 images," *IEEE J. Sel. Topics Appl. Earth Observ. Remote Sens.*, vol. 9, no. 4, pp. 1331–1342, Apr. 2016.
- [68] J. S. Lee, D. L. Schuler, T. L. Ainsworth, and W.-M. Boerner, "Polarization orientation estimation and applications: A review," in *Proc. IEEE Int. Geosci. Remote Sens. Symp. (IGARSS)*, vol. 1, Jul. 2003, pp. 428–430.
- [69] L. Jong-Sen, D. L. Schuler, and T. L. Ainsworth, "Polarimetric SAR data compensation for terrain azimuth slope variation," *IEEE Trans. Geosci. Remote Sens.*, vol. 38, no. 5, pp. 2153–2163, Sep. 2000.



Guo-Hui Yao received the B.S. degree in geoscience from Suzhou University, Suzhou, China, in 2013, and the M.S. degree in ecology from Xinjiang Agricultural University, Ürümqi, China, in 2016. She is currently pursuing the Ph.D. degree in geography with the School of Geography and Ocean Science, Nanjing University, Nanjing, China.

Her research interests include the application of microwave remote sensing in urban and cryosphere.



Chang-Qing Ke received the B.S. degree in geography from Shaanxi Normal University, Xi'an, China, in 1993, the M.S. degree in geography from the Lanzhou Institute of Glaciology and Geocryology, Chinese Academy of Sciences, Lanzhou, China, in 1996, and the Ph.D. degree from the Nanjing Institute of Geography and Limnology, Chinese Academy of Sciences, Nanjing, China, in 1999.

From 1999 to 2002, he was a Post-Doctoral Research Fellow with the School of Geography and Ocean Science, Nanjing University, Nanjing, where

he has been an Associate professor and a Full Professor in remote sensing since 2002 and 2007, respectively. His research interests include satellite image processing, remote sensing of cryosphere and water resource, and climate change.



Xiaobing Zhou received the B.S. degree in physics from Hunan Normal University, Changsha, China, in 1986, the M.S. degree in theoretical physics from Sichuan University, Chengdu, China, in 1989, and the Ph.D. degree in geophysics with specialization in remote sensing from the University of Alaska Fairbanks, Fairbanks, AK, USA, in 2002.

He was with the Southwestern Institute of Physics, Chengdu, as a Research Assistant Professor from 1989 to 1995 and a Research Associate Professor from 1995 to 1997; with the University of California at San Diego, San Diego, CA, USA, as a Visiting Scientist in 1997; with the Institute of Geophysics, University of Alaska, as a Visiting Scientist in 1998; with New Mexico Tech, Socorro, NM, USA, as a Research Assistant Professor from 2002 to 2005; and has been with the Department of Geophysical Engineering, Montana Tech of The University of Montana, Butte, MT, USA, as an Assistant Professor, an Associate Professor, and a Full Professor in geophysical engineering since 2005, 2009, and 2014, respectively. His research interests include remote sensing theories, algorithm development, instrumentation (optical remote sensing and imaging radar), image data collection and processing, and applications in earth and environmental sciences, including geophysical exploration.



Hoonyol Lee (S'99–M'01–SM'11) was born in Gwangju, South Korea, in 1969. He received the B.S. degree in geology and the M.S. degree in geophysics from the Department of Geological Sciences, Seoul National University, Seoul, South Korea, in 1995 and 1997, respectively, and the Ph.D. degree in radar remote sensing from the Department of Earth Sciences and Engineering, Imperial College London, University of London, London, U.K., in 2001.

From 2001 to 2003, he was a Post-Doctoral Research Associate with Imperial College London. From 2003 to 2004, he was a Senior Researcher with the Korea Institute of Geoscience and Mineral Resources (KIGAM), Daejeon, South Korea. He was a Visiting Scholar with the Department of Geological Sciences, University of Oregon, Eugene, OR, USA, from August 2008 to July 2009, and with the Department of Civil, Environmental, and Construction Engineering, University of Central Florida, Orlando, FL, USA, from August 2014 to July 2015. Since 2004, he has been with the Department of Geophysics, Kangwon National University, Chuncheon, South Korea, where he is currently a Professor. His research interests include synthetic aperture radar, interferometry, and polarimetry for earth science and cryosphere study. He developed an educational synthetic aperture radar (eSAR) processor, an SAR ocean processor (SOP), polarimetric scatterometer systems, and ground-based SAR systems.

Dr. Lee is a Senior Member of the IEEE Geoscience and Remote Sensing Society and a member of the American Geophysical Union. He received the Interactive Session Prize Paper Award at the 1999 IEEE International Geoscience and Remote Sensing Symposium (IGARSS'99), Hamburg, Germany, and the Best Paper Award of the *Korean Journal of Remote Sensing* in 2008. From 2011 to 2013, he served as the Editor-in-Chief of the *Korean Journal of Remote Sensing*. He has been the Vice-President of the Korean Society of Remote Sensing since 2017.



Xiaoyi Shen received the B.S. degree from the School of Remote Sensing, Nanjing University of Information Science and Technology, Nanjing, China, in 2015, and the M.S. degree from the School of Geography and Ocean Science, Nanjing University, Nanjing, in 2018, where he is currently pursuing the Ph.D. degree.

His research interests include satellite image processing, remote sensing of cryosphere, and polar climate change.



Yu Cai received the B.S. degree in geography from Nanjing University, Nanjing, China, in 2012, where she is currently pursuing the Ph.D. degree in geography with the School of Geography and Ocean Science.

Her research interests include remote sensing and lake-atmosphere interaction.